Transport properties of (Bi,Sb)$_2$Te$_3$ topological insulator crystals with lateral p-n junction

V. A. Golyashov [1,2,3,*] K. A. Kokh,[4] and O. E. Tereshchenko [1,2,3]

[1]*Rzhanov Institute of Semiconductor Physics, Siberian Branch, Russian Academy of Sciences, Novosibirsk 630090, Russia*
[2]*Synchrotron Radiation Facility SKIF, Boreskov Institute of Catalysis, Siberian Branch, Russian Academy of Sciences, Kol'tsovo 630559, Russia*
[3]*Novosibirsk State University, Novosibirsk 630090, Russia*
[4]*Sobolev Institute of Geology and Mineralogy, Siberian Branch, Russian Academy of Sciences, Novosibirsk 630090, Russia*

High-quality low-bulk-carrier-concentration 3D topological insulator crystals and films are required for the majority of their potential applications. Creating a p-n transition using composition grading is one of the ways to obtain compensated regions in the bulk of 3D topological insulator crystals. Eventual formation of a p-n junction in 3D topological insulator surface states is expected to enhance the surface-transport-related spin filtering and charge-to-spin conversion. Here we report a detailed study of the transport and surface electronic structure of composition-graded Bi$_2$Te$_3$ and Bi$_{1.34}$Sb$_{0.66}$Te$_3$ single crystals with built-in lateral p-n transition. The defect compensation naturally achieved at the p-n interface results in a strong reduction of the bulk carrier concentrations in both crystals. In the Bi$_2$Te$_3$ crystal a high-mobility n-type conductivity region is formed with electron Hall mobility of 70 000 cm^2 V^{-1} s^{-1} and Hall concentration of 2×10^{18} cm^{-3} at 4.2 K. In the Bi$_{1.34}$Sb$_{0.66}$Te$_3$ crystal the region of intrinsic conductivity with the lowest observed hole Hall concentration of 6×10^{17} cm^{-3} and hole Hall mobility of 10 000 cm^2 V^{-1} s^{-1} is formed in the vicinity of the p-n junction. The downward band bending was observed on the surface of the p-type conductivity region of the Bi$_2$Te$_3$ and Bi$_{1.34}$Sb$_{0.66}$Te$_3$, providing an almost barrierless topological surface state electron channel with no topological p-n junction formed. The composition grading can be used as a reliable method of obtaining high-quality single crystals with relatively large areas of low bulk carrier concentrations and enhanced charge carrier mobility, which can be used in further nanoscale topological insulator device fabrication.

I. INTRODUCTION

Tetradymite-type V-VII compounds (Bi$_2$Te$_3$, Sb$_2$Te$_3$, Bi$_2$Se$_3$, etc.) have been widely studied for the last 60 years as good thermoelectric materials for room temperature applications [1,2]. Recently, these compounds were found to be three-dimensional topological insulators (TIs): due to strong spin-orbit interaction and nontrivial bulk band structure they possess metallic topological surface states (TSSs) [3–7]. The TSSs have a quasilinear dispersion in the form of a single Dirac cone with helical spin texture and are topologically protected from backscattering by a time-reversal symmetry. This property of TSSs makes them a promising platform for studying spin-dependent phenomena and creating new spintronics devices, as well as observing Majorana fermions, the topological superconducting proximity effect, and the topological magnetoelectric effect [8].

TSSs of the 3D TIs can be easily observed using angle-resolved photoelectron spectroscopy (ARPES) or scanning tunneling microscopy (STM). However, the low formation energy of electrically active point defects [9] leads to a high concentration of free charge carriers in the bulk of these materials (usually on the order of 10^{19} cm^{-3}) and makes it impossible to separate the transport properties of the TSSs from the conductivity of the bulk. This problem can be partially solved by the creating a few quintuple-layer thin TI films [10] together with external doping [4,11–13], or selection of compensated quaternary compositions of Bi$_{2-x}$Sb$_x$Te$_{3-y}$Se$_y$ crystals and films [14–16] at the expense of introduction of additional disorder into the system and enhancement of impurity scattering. Different approaches of probing transport properties of TSSs may include formation of the p-n junction in the bulk of TI crystals. Creating a p-n junction for charge carriers on topological surface states is of special interest. Such "topological" p-n junction is a natural boundary for the emergence of TSS edge modes in strong magnetic fields [17,18]. It was shown theoretically that the combination of spin-momentum locking in TSSs and momentum filtering at the p-n junction results in efficient spin filtering and charge-to-spin conversion [19], tuned either magnetically [20] or electrostatically [18,21], during surface transport through the interface, thus leading to the topological p-n junction being a promising system for implementing a spin transistor [20,22,23].

It is known that Bi$_2$Te$_3$ conductivity type is determined by the presence of acceptor Bi$_{Te}$ or donor Te$_{Bi}$ antisite defects. Antisite formation energies depend on the Bi-Te stoichiometric ratio [9]. This fact means that conductivity type and carrier concentration of Bi$_2$Te$_3$ crystals grown by the Bridgman method can be controlled via changing the concentration

---
*golyashov@isp.nsc.ru

of Te atoms in the initial growth melt within the 60%–63% range [24–26]. Thus, in paper [27] it was reported obtaining intrinsic n-Bi_2Te_3 crystals from $Bi_{1.85}Te_{3.15}$ melts with electron concentration $n = 3 \times 10^{17}$ cm^{-3} and mobility $\mu_H = 1.8 \times 10^5$ cm^2 V^{-1} s^{-1} at $T = 4.2$ K. Also, the inevitable rise of the tellurium concentration in the melt during crystal growth can lead to formation of the built-in lateral p-n junction (the p-n junction is formed in the plane of bismuth telluride quintuple layers) in the direction of crystallization [28,29]. Formation of a lateral p-n junction during crystal growth was also reported for the $(Bi, Sb)_2Te_3$ [30] and $Bi_2(Te,Se)_3$ solid solutions [13,31]. However, in the case of the $Bi_2(Te,Se)_3$ system, multiple crystal phases were formed due to the specific features of the embedding of Se and Te atoms into the crystal lattice. A perpendicular p-n junction (the p-n junction is directed along the c axis of the tetradymite crystal structure normal to the quintuple layers) was obtained by annealing of p-Bi_2Te_3 in Se vapor [32], by deposition of Sb bilayers on the surface of n-Bi_2Se_3 [33], and in epitaxial Sb_2Te_3/Bi_2Te_3 heterostructures [34,35]. Interesting results were obtained when p-n junctions were created using the field effect in thin compensated TI films using electrostatic gating [18], organic molecules [36], or electrolytes [12] to control the surface band bending. The built-in p-n junctions in composition-graded 3D TI crystals are of interest because the chemical potential in them should, formally, change smoothly between parts of p- and n-type conductivity. So, one can expect the presence of an extended region of intrinsic conductivity, or a compensated region, at the vicinity of the p-n junction. We have already shown [28] that in Bi_2Te_3 crystals with the p-n transition, low carrier concentration $n = 2 \times 10^{17}$ cm^{-3} can be achieved, studied the distribution of point defects in such crystal, and found the p-n junction width to be ~40 nm [29]. In this paper, we present a more detailed study of the transport properties and surface electronic structure of Bi_2Te_3 and $(Bi,Sb)_2Te_3$ crystals with built-in lateral p-n transition near the region of conductivity-type change.

II. MATERIALS AND METHODS

Bi_2Te_3 and $Bi_{2-x}Sb_xTe_3$ compounds were synthesized by direct alloying of elemental Bi (99.999%), Te (99.99%), and Sb (99.99%). The charge of elemental components with given stoichiometric ratios was sealed into the quartz ampoules evacuated to ~10^{-4} mbar and melted by heating to a temperature higher than the melting temperature by 20 K. The melt was kept at this temperature for 24 hours for homogenization. The resulting polycrystalline ingots were recrystallized using a modified vertical Bridgman-Stockbarger method with a rotating heat field [37] in quartz ampoules evacuated to ~10^{-4} mbar with pyrolytic carbon lining deposited on the inner walls and an extended conical bottom. The crystallization took place under quasiequilibrium conditions with crystallization front velocity ~5 mm/day in the temperature gradient ~1 K/mm. The result was crystals consisting of one or more large monocrystalline blocks [Fig. 1(e)], with axis c perpendicular to the growth axis. The atomic composition of the crystal grown was controlled using energy-dispersive x-ray spectroscopy (EDX).
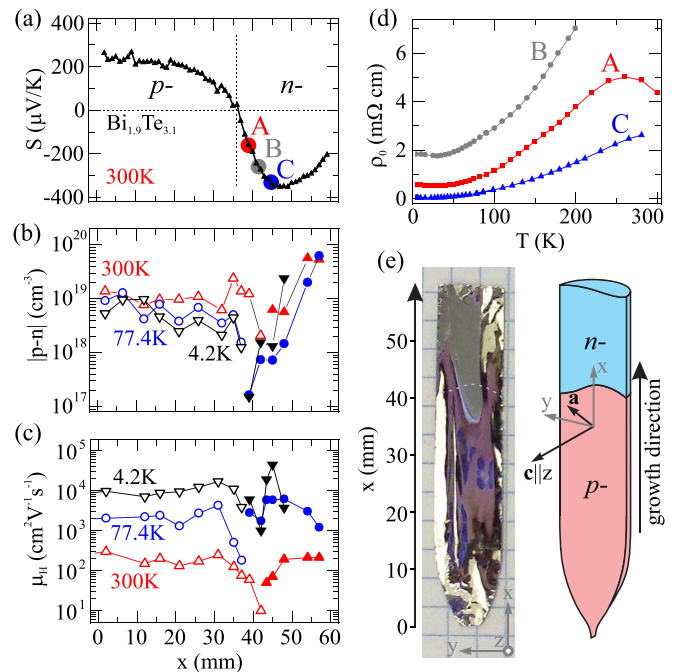
FIG. 1. Seebeck coefficient (a), Hall concentration (b), and Hall mobility (c) values measured along the growth axis of the Bi_2Te_3 crystal. Blank symbols are for holes; filled symbols are for electrons. Point $x = 0$ mm corresponds to the lowest part of the growth boule. (d) Resistivity temperature dependencies for samples taken at points A, B, and C of the crystal in (a). (e) Schematic image and photo of the Bi_2Te_3 slab cleaved from the single crystal. **a** and **c**: directions of the crystal hexagonal axes.

For further measurements, 0.5–1 mm thick slabs were cleaved from the crystals along the (0001) plane. The Seebeck coefficient was measured using two copper probes with a temperature difference of 5 K spaced 1 mm apart. A part of the transport measurements was made using the four-contact van der Pauw method, with sample dimensions of about $2 \times 2 \times 0.1$ mm and indium solder contacts. For detailed magnetotransport measurements, samples with dimensions of about $5 \times 1 \times 0.1$ mm were cut from the slabs with the long side perpendicular to the crystallization direction, and six indium contacts were soldered along their perimeter in standard Hall bar geometry. The longitudinal resistance ρ_{xx} and the Hall resistance ρ_{xy} were measured using the standard lock-in technique with an AC excitation current of 100 µA and 137 Hz in a perpendicular magnetic field up to ± 2 T. Hall concentrations and mobilities were calculated using unity Hall factor.

The surface electronic structure was studied using angle-resolved photoemission spectroscopy (ARPES). The data were acquired at the UE112-PGM1 line of the BESSY II Synchrotron Radiation Center (Berlin, Germany) and at the ISP SB RAS (Novosibirsk, Russia) using a laboratory setup equipped with a nonmonochromated He-discharge UV source. The (0001) surface was prepared by cleaving samples directly in the vacuum chamber of the electron spectrometer under ultrahigh vacuum conditions ($<5 \times 10^{-10}$ mbar) at room temperature. The measurements were made using a photon energy of 23 eV or 21.22 eV at a sample temperature of 30 K.

III. RESULTS AND DISCUSSION

A. The p-n transition in Bi$_2$Te$_3$

Bi$_2$Te$_3$ single crystals with a diameter of 12 mm and total length of ~ 60 mm were obtained by the vertical Bridgman method from melts with Bi$_{1.9}$Te$_{3.1}$ composition (2% excess tellurium). The crystals were easily cleaved in slabs [Fig. 1(e)] along the quintuple layers' (0001) plane parallel to the growth axis x. The value of $x = 0$ mm corresponds to the conical end of the crystal (conical bottom of the quartz ampoule), where the crystal growth started. Slabs cleaved close to the central part of the crystals were taken for electrical property measurements. EDX measurements showed that the crystal atomic composition is close to the Bi$_2$Te$_3$ stoichiometry, with slightly increasing Te/Bi ratio along the crystal growth direction.

The value of the Seebeck coefficient [Fig. 1(a)] changes continuously along the growth axis of the obtained crystal, and changes its sign from positive to negative at $x \sim 35$ mm, indicating a change from hole to electronic conductivity type at the point with $S = 0\ \mu$V/K. The value of the Seebeck coefficient in the first part of the crystal ($x \sim 0$–25 mm) changes smoothly in the range of 200–250 μV/K and corresponds to the expected values for highly doped p-Bi$_2$Te$_3$ [38]. In the electronic part of the obtained crystal the absolute value of S grows rapidly and S reaches a minimum of $S = -350$ Bi$_2$Te$_3$ at $x \approx 47$ mm. Such a large value of the Seebeck coefficient for n-Bi$_2$Te$_3$ is not typical, but is theoretically expected for weakly doped Bi$_2$Te$_3$ crystals [39].

Figures 1(b) and 1(c) show the distributions of the Hall concentration and carrier Hall mobility along the growth axis of the Bi$_2$Te$_3$ crystal at different temperatures. The Hall coefficient changes its sign from positive to negative at $x \approx 38$ mm.

The obtained crystal can be conventionally divided into three parts. In the first part ($x = 0$–30 mm) a high hole concentration $p = (5$–$10) \times 10^{18}$ cm^{-3} is observed. Hole Hall mobility reaches $\mu_h \approx 300$ cm^2 V^{-1} s^{-1} at room temperature and increases up to $\mu_h \approx 12\,000$ cm^2 V^{-1} s^{-1} at 4.2 K, indicating overall good quality of the crystal grown. The second part of the crystal ($x = 30$–43 mm) contains the region of carrier-type change. There is a change of carrier type from holes to electrons at point $x \approx 38$ mm. Minimal Hall concentration reaches $n \approx 2 \times 10^{17}$ cm^{-3} at $T = 4.2$ K. However, mobility of carriers in this point is also minimal with $\mu_e \approx 3000$ cm^2 V^{-1} s^{-1}. This indicates that an impurity compensation takes place in this part of the crystal, but the total concentration of defects remains high. It is interesting that the sign of the Seebeck coefficient in this part of the crystal remains positive, which confirms the assumption of the compensation. In the third part of the crystal ($x = 43$–46 mm) the electron concentration remains low $n \approx 2 \times 10^{18}$ cm^{-3}, but there is a significant increase in electron Hall mobility to the value $\mu_e \approx 70\,000$ cm^2 V^{-1} s^{-1}. This area also corresponds to the highest absolute value of the Seebeck coefficient. The rapid growth of carrier concentration at the end of the crystal ($x > 46$ mm) can be caused by an increase in the number of defects due to the excessive tellurium content in the growth melt at the end of crystal growth.

Formation of the p-n junction is determined by phase diagram of the Bi-Te (or the Bi-Sb-Te) system and the way the initial melt follows it during the crystal growth process. The
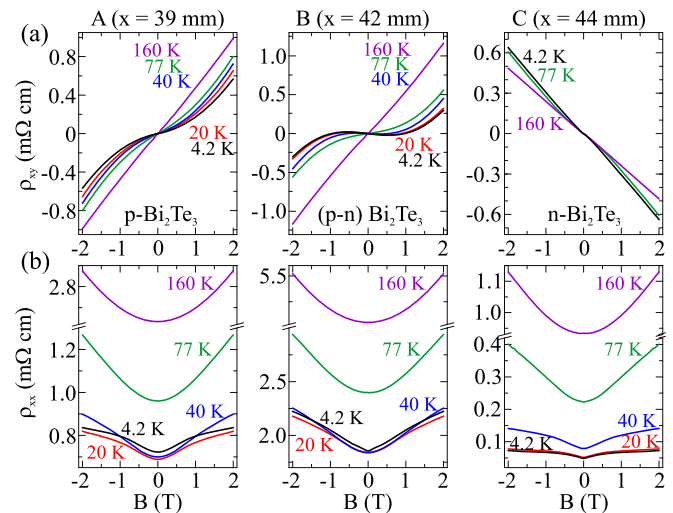
FIG. 2. Hall resistance ρ_{xy} (a) and magnetoresistance ρ_{xx} (b) for the samples taken in points A, B, and C of the Bi$_2$Te$_3$ crystal, shown in Fig. 1(a), at different temperatures.

latter depends on the initial melt stoichiometry, the exact size and shape of the quartz ampoules used, and the crystallization process details. We have found that in our Bridgman furnace the position of the p-n junction in different Bi$_2$Te$_3$ crystals is almost the same and can be predicted with an accuracy of ~ 5 mm. The moment of the p-n junction formation in the crystal corresponds to the exact composition of the melt it is crystallized from. The p-n transition is expected to occur in a single moment of time across all the crystallization front. The crystallization front shape is not a plane, but some curved surface that depends on the temperature distribution in the furnace and the crystal-melt system. Probing the Seebeck coefficient sign in different parts of the crystal at room temperature we found it to be bent to the end of the crystal in its central part by ~ 2 mm as is schematically shown in Fig. 1(e). We did not find any preferred direction of the crystal quintuple-layer hexagonal axes with respect to the growth direction in the different crystals obtained, and can conclude that the quintuple-layer hexagonal axes are randomly aligned with respect to the p-n junction. However, it should be noted that the p-n junction boundary is curved, so if it is measured using the scanning Seebeck probe and the crystal crystallographic directions are determined using x-ray or electron diffraction, the parts of the crystal with almost any specific hexagonal axes to p-n junction alignment can be chosen.

In order to study crystal properties in areas of the compensation and the adjacent high-mobility n-type region, the Hall-bar samples were taken from the second and third parts of the crystal at points A, B, and C shown in Fig. 1(a). In all three points chosen the resistivity temperature dependencies [Fig. 1(d)] are conventionally metallic. However, at temperatures less than 30 K a weak increase in resistivity with decreasing temperature is observed for the samples A and B, and the dependence shows weak semiconducting behavior.

Measured magnetic field dependencies of the Hall resistance $\rho_{xy}(B)$ and magnetoresistance $\rho_{xx}(B)$ for the samples A, B, and C are shown in Fig. 2. At 160 K and above the dependencies of resistance ρ_{xy} on the magnetic field are linear

TABLE I. Drude fit parameters for $\rho_{xy}(B)$ and $\rho_{xx}(B)$ for samples A, B, and C at 4.2 K and 77 K.

	Sample	A	B	C
		$T = 4.2$ K		
p	cm^{-3}	2.3×10^{18}	2.5×10^{18}	1.8×10^{17}
μ_h	$\text{cm}^2\,\text{V}^{-1}\,\text{s}^{-1}$	3300	1100	55000
n	cm^{-3}	8×10^{16}	7×10^{16}	2.3×10^{18}
μ_e	$\text{cm}^2\,\text{V}^{-1}\,\text{s}^{-1}$	13000	8300	53000
		$T = 77$ K		
p	cm^{-3}	1.3×10^{18}	1.1×10^{18}	4×10^{17}
μ_h	$\text{cm}^2\,\text{V}^{-1}\,\text{s}^{-1}$	4200	1800	7700
n	cm^{-3}	1.6×10^{17}	1.1×10^{17}	2×10^{18}
μ_e	$\text{cm}^2\,\text{V}^{-1}\,\text{s}^{-1}$	6500	5300	12000

FIG. 3. Hall concentration (a) and Hall mobility (b) temperature dependencies for n-Bi_2Te_3 [sample from point C in Fig. 1(a)]. (c) Hall resistance ρ_{xy} and magnetoresistance ρ_{xy} of n-Bi_2Te_3 sample near point C and (d) the second derivative $d^2\rho_{xx}/dB^2$. The inset shows FFT results on $d^2\rho_{xx}/dB^2$ vs $1/B$ curve in a range of $B = 1.5$ T to 10 T.

and reveal p-type conductivity for the samples A and B, and n-type conductivity for the sample C. As noted above, there is some discrepancy between the sign of the Hall coefficient and the sign of the Seebeck effect, which may indicate the presence of several types of charge carriers in the samples studied. The value of the positive magnetoresistance corresponds to the geometric magnetoresistance $\Delta\rho_{xy}(B) \sim \mu^2 B^2$.

As the temperature decreases, $\rho_{xy}(B)$ becomes strongly nonlinear in samples A and B. At 4.2 K, $\rho_{xy}(B)$ for the sample B becomes negative in low magnetic fields, and its magnetic field dependence becomes sign-variable, clearly indicating the presence of both holes and electrons of comparable concentrations in this part of the Bi_2Te_3 crystal. The magnetoresistance $\rho_{xx}(B)$ becomes nonparabolic in all the studied samples at temperatures below 77 K, with a characteristic quasilinear dependence on the magnetic field in the low-field region at 4.2 K. The linear magnetoresistance is frequently observed in 3D TIs and is usually related to the appearance of the weak-antilocalization effect [40], expected for transport along the surface states. On the other hand, nonparabolic magnetoresistance can be explained by the inhomogeneous distribution of carrier concentrations and mobilities in the samples under investigation. Similar dependencies have already been observed in semimetals and disordered systems [41,42]. In our case, because of the large (0.1–0.2 mm) thickness of the samples investigated, we could expect negligibly small contribution of TSSs in the low-field data measured.

The $\rho_{xy}(B)$ and $\rho_{xx}(B)$ dependencies were fitted using a two-component (electrons and holes) Drude model. The best-fit values of concentrations and mobilities for 4.2 K and 77 K temperatures are given in Table I.

The presence of composition and, as a result, chemical potential fluctuations in the crystal is probably the main reason for the relatively high concentration of both types of charge carriers in the crystal. At $T = 4.2$ K, hole concentrations in samples A and B are almost identical. The concentration of holes is more than one order of magnitude higher than for electrons. Since the mobility of electrons is much higher than that of holes, hole and electron contributions to conductivity are comparable. The decrease in carrier mobility at point B, corresponding to the region of the crystal with a p-n junction, is probably due to increase of the total number of the point defects at the vicinity of the p-n transition region as was seen

previously in STM measurements [29]. In sample C the main charge carriers are electrons; the concentration of holes is an order of magnitude smaller, but both electrons and holes have high mobility $\mu_{e,h} \approx 53\,000$ $\text{cm}^2\,\text{V}^{-1}\,\text{s}^{-1}$. The increase in mobility in the n-type region, while preserving a large total carrier concentration, is probably due to the charged-impurity screening by high-mobility free carriers [43]. It can be noted that a decrease in the concentration of primary carriers with an increase in the concentration of minor carriers is observed in all the samples studied when the temperature raised to 77 K, with the mobility of holes in samples A and B increased. Temperature dependencies of the Hall concentration and mobility of sample C are shown in Figs. 3(a) and 3(b). It is seen that the electron concentration decreases as the temperature decreases to 60 K, reaches a minimum of $n \sim 2 \times 10^{18}$ cm^{-3}, and then practically does not change until 4.2 K. The Hall mobility of electrons remains constant from 4.2 K to 30 K and reaches the value $\sim 70\,000$ $\text{cm}^2\,\text{V}^{-1}\,\text{s}^{-1}$. It can be assumed that at $T < 30$ K the mobility is limited due to neutral impurity scattering. The temperature dependence of mobility at $T > 30$ K follows the law $\mu \sim T^{-2.2}$ and can be connected to joint acoustic and optical phonon deformation potential scattering [44]. The properties of the Bi_2Te_3 crystal near point C are similar to those obtained in [24,27] on n-Bi_2Te_3 crystals.

Figure 3(c) shows magnetic field dependencies of Hall resistance $\rho_{xy}(B)$ and magnetoresistance $\rho_{xy}(B)$ for the sample taken between points B and C of the Bi_2Te_3 crystal measured in high perpendicular magnetic fields at 4.2 K. The sample has n-type conductivity with $n \approx 1 \times 10^{18}$ cm^{-3} and $\mu_e \approx 30\,000$ $\text{cm}^2\,\text{V}^{-1}\,\text{s}^{-1}$ at liquid helium temperature. It is seen that $\rho_{xy}(B)$ remains linear up to 10 T while $\rho_{xy}(B)$ shows quasiparabolic dependence on B with a pronounced Shubnikov–de Haas (SdH) oscillation pattern, related to Landau level quantization, at $B > 2$ T. As is seen in Fig. 3(d), showing the second derivative of the $\rho_{xy}(B)$ curve, the oscillations are

periodic in inverse magnetic field and have a beating pattern, indicating the presence of several sets of Landau levels. FFT analysis of the SdH oscillations [inset in Fig. 3(d)] reveals two frequencies $f_1 = 12.8$ T and $f_2 = 23.6$ T with corresponding values of Fermi wave vectors $k_{F1} = 2 \times 10^6$ cm^{-1} and $k_{F2} = 2.7 \times 10^6$ cm^{-1}. The presence of two SdH frequencies in 3D TI samples is usually referred to joint contribution of high-mobility bulk and surface channels to conductivity [45,46]. The dimensionality of the effect observed and effective mass of the charge carriers contributing to it can be probed by angle and temperature analysis of the SdH oscillations, but that is outside the scope of this study, so we cannot attribute frequencies measured to the certain channel. The coexistence of multiple carriers makes it difficult to identify the set of Landau levels for each part to distinguishing the surface state Dirac fermions from the bulk carriers. However, since the calculated k_F values are close to each other, we can evaluate the electron densities of 2D and 3D channels as $n_{2D} = 3$–6×10^{11} cm^{-2} and $n_{3D} = 4$–9×10^{18} cm^{-3}. The latter value is close to the bulk electron concentration derived from low-field Hall measurements. As no 2DEG states are formed on the n-type Bi$_2$Te$_3$ sample surface, the 2D channel can, in principle, be attributed to topological surface states formed on the top and bottom sample surfaces.

Despite the existence of the p-n junction in the crystal bulk, the samples taken from the p-n junction region do not exhibit any rectifying properties. Instead of N-shaped tunnel diode voltage-current characteristics, a linear voltage-current dependency was observed, with a characteristic value of electrical resistance $\sim$1 ohm (for a sample size of $\sim 10 \times 1 \times 0.1$ mm). This can be related to the large lateral extent, or insufficient homogeneity of the obtained p-n junction, in the vertical direction also.

B. The p-n transition in Bi$_{2-x}$Sb$_x$Te$_3$

To investigate the possibility of obtaining a bulk p-n junction in the Bi$_{2-x}$Sb$_x$Te$_3$ system, two crystals were grown from melts with initial compositions of Bi$_{1.34}$Sb$_{0.66}$Te$_3$ and Bi$_{0.8}$Sb$_{1.2}$Te$_3$ with 2% of excess Te added. It was expected that the p-n junction would be realized during growth of the Bi$_{0.8}$Sb$_{1.2}$Te$_3$ crystal, but the obtained crystal turned out to be entirely of p-type conductivity. The distribution of the Seebeck coefficient values measured along the growth axis of Bi$_{1.34}$Sb$_{0.66}$Te$_3$ crystals at room temperature is shown in Fig. 4(a). The change in the sign of the Seebeck coefficient in the Bi$_{1.34}$Sb$_{0.66}$Te$_3$ crystal from positive to negative occurs at a distance of $\sim$50 mm from the beginning of the crystal and points to a change in the conductivity type from hole to electronic and, accordingly, to the presence of a built-in lateral p-n junction in this region of the crystal. In contrast to the p-n junction in Bi$_2$Te$_3$ the maximum absolute values of the Seebeck coefficient are reached near the boundary of the p-n junction and are 290 µV/K and -270 µV/K for the p and n regions of crystals, respectively. The atomic composition Bi$_{1.34}$Sb$_{0.66}$Te$_3$ crystal was found to gradually change along the crystal growth direction with the Bi/Sb ratio increased from 1.7 to 2.3 between the crystal tip and end with stoichiometry being close to Bi$_{2-x}$Sb$_x$Te$_3$.
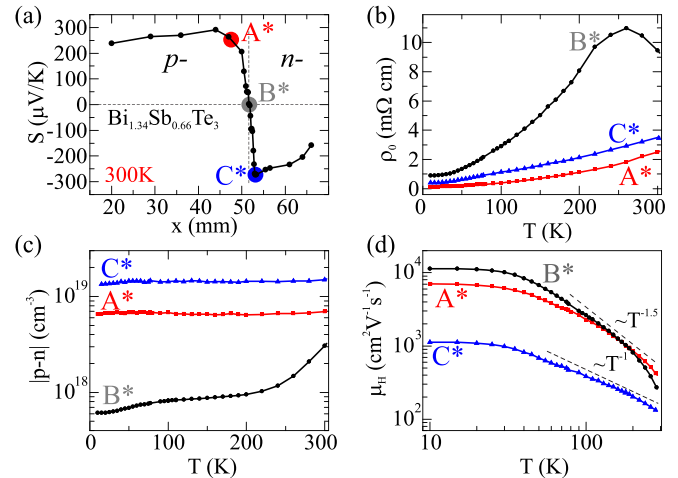
FIG. 4. (a) Distribution of Seebeck coefficient along the growth axis of the Bi$_{1.34}$Sb$_{0.66}$Te$_3$ crystal. (b), (c), and (d) Temperature dependencies of the resistivity, Hall concentration, and mobility of charge carriers at the specified points A*, B*, and C* of the Bi$_{1.34}$Sb$_{0.66}$Te$_3$ crystal.

For a detailed study of the Bi$_{1.34}$Sb$_{0.66}$Te$_3$ crystal's galvanomagnetic properties, samples were taken at points A*, B*, and C* shown in Fig. 4(a) close the p-n junction region. The temperature dependencies of resistivity [Fig. 4(b)] in all three points show a metallic character, but the magnitude of the resistance change and its absolute value in point B, directly corresponding to the p-n junction region, was the largest.

In the samples studied, no strong nonlinearity of the Hall effect was observed, so only the values of the Hall concentration and mobility were calculated. Their temperature dependencies are shown in Figs. 4(c) and 4(d). The hole concentration at point A* is $p = 6.5 \times 10^{18}$ cm^{-3} and is practically independent of temperature. At point B* the carrier concentration decreases with temperature from $p = 3 \times 10^{18}$ cm^{-3} at room temperature to $p = 6 \times 10^{18}$ cm^{-3} at 4.2 K. The maximum mobility of holes in sample A* is $\mu_h \sim 7000$ cm^2 V^{-1} s^{-1}, while at point B* the maximum mobility increases to $\mu_h \sim 10\,000$ cm^2 V^{-1} s^{-1}. At $T > 30$ K, the carrier mobility in sample B* changes as $\mu \sim T^{-3/2}$, which corresponds to carrier scattering on the acoustic phonon deformation potential. It can be assumed that sample B is compensated, but the relatively large mobility of holes contradicts this. In the temperature dependence of concentration two kinks are observed at $T \sim 60$ K and $T \sim 230$ K, corresponding to activation energies $E_1 \sim 1.5$ meV and $E_2 \sim 110$ meV. E_2 corresponds to the expected band gap width of Bi$_{1.34}$Sb$_{0.66}$Te$_3$. In the sample C* a very high concentration of electrons $n \sim 1.4 \times 10^{18}$ cm^{-3} and a decrease in mobility to $\sim$1000 cm^2 V^{-1} s^{-1} is observed. The temperature dependencies of mobility for the both samples A* and C* are close to $\mu \sim T^{-1}$ at $T > 30$ K, indicating possible simultaneous contribution of charged impurity, alloy disorder, and phonon scattering due to higher carrier and point defect concentrations compared to sample B*.

The magnetic field dependencies $\rho_{xy}(B)$ and $\rho_{xy}(B)$ for the points A*, B*, and C* of the Bi$_{1.34}$Sb$_{0.66}$Te$_3$ crystal (Fig. 5)
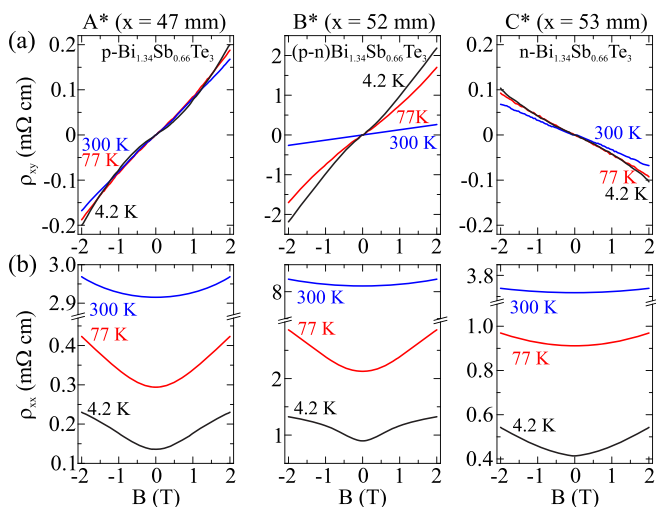
FIG. 5. Hall resistance and magnetoresistance at points A*, B*, and C* of $Bi_{1.34}Sb_{0.66}Te_3$ crystal, shown in Fig. 4(a), at different temperatures.

show a strong positive magnetoresistance and weak nonlinearity of the Hall effect, indicating the presence of several charge carrier groups, which can be related to the presence of inhomogeneities in the studied samples. In sample B* a strong increase of ρ_{xy} value with decreasing temperature is observed, and at $T = 4.2$ K, the value of ρ_{xy} exceeds that for other samples by an order of magnitude.

The results obtained for the $Bi_{1.34}Sb_{0.66}Te_3$ crystal with a p-n junction are generally similar to those obtained for Bi_2Te_3 crystals. It can be noted that in the region of the p-n junction in this crystal there is a high-mobility region of conventionally intrinsic conductivity. However, introduction of the third component into the solid solution inevitably leads to the increase of disorder in the system, and the maximum values of charge carrier mobility are generally lower than in Bi_2Te_3 crystals.

C. Surface electronic structure of (Bi, Sb)₂Te₃ crystals

The studied crystals contain a p-n transition in their bulk, but the question of the existence of a "topological" p-n junction on their surface requires a separate study. To answer this question the electronic structure of the obtained crystal's surfaces was studied by the ARPES method. To exclude the influence of atmospheric gas adsorption, the samples were cleaved directly in an ultrahigh-vacuum ($<5 \times 10^{-10}$ mbar) spectrometer chamber. The band dispersion dependencies obtained at two points of the same (0001) Bi_2Te_3 cleaved surface in two regions of different conductivity types are shown in Figs. 6(a) and 6(b). The spectra obtained in the p- and n-type conduction crystal regions in the bulk are almost identical: at binding energies of 0 to 140 meV, two branches of linear-dispersion topological surface states (TSSs) are visible. The Dirac point (DP) position can be estimated around ~ 200 meV below the Fermi level for both points. At binding energies above 140 meV, the M-shaped dispersion of valence band (VB) states is observed. The Fermi level on the surface (0001) of the crystal after cleaving in ultrahigh vacuum in both the n and p regions is slightly below the conduction band minimum,
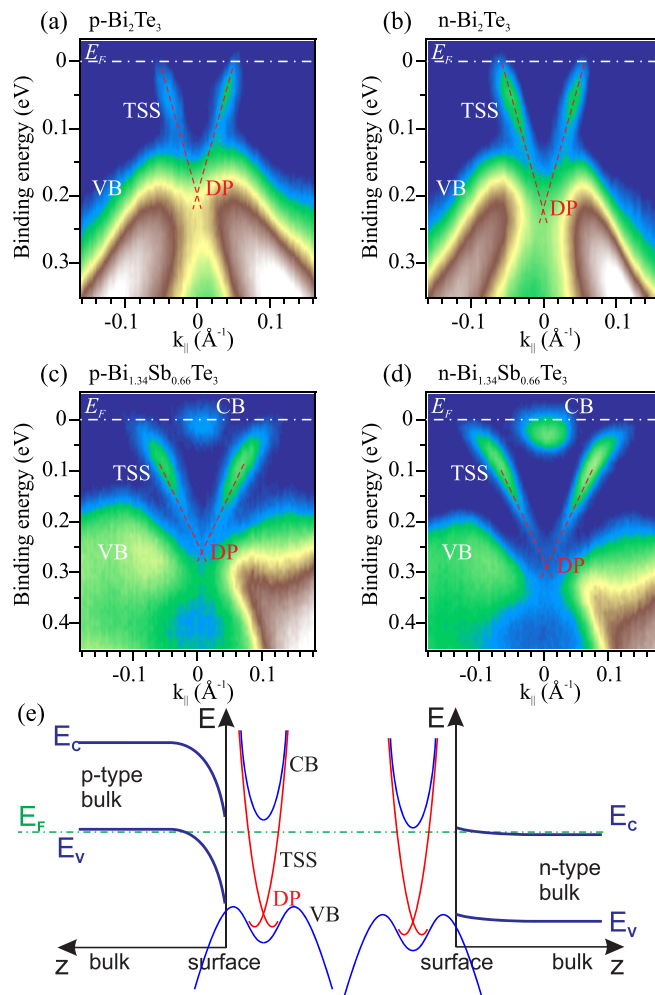
FIG. 6. Dispersion dependencies measured by ARPES for the surface (0001) in (a) p and (b) n regions of Bi_2Te_3 crystal and (c) p and (d) n regions of $Bi_{1.34}Sb_{0.66}Te_3$ crystal (G-K direction, $h\nu = 23$ eV, $T = 30$ K). (e) Schematic band diagrams of the space charge regions on the surface of the Bi_2Te_3 crystal in the p- and n-type regions, respectively. TSS: TI surface states with Dirac point at DP; VB: valence band states; CB: conduction band states.

which means that a surface band bending occurred at least in the p-type part of the crystal. It can be assumed that even in bulk p-type samples surface electron channels related to topological surface states and surface 2DEG can be found to contribute to conductivity. However their relative contribution could depend strongly on a variety of experimental factors.

Schematic band diagrams of the space charge region formed on the p- and n-type regions of the Bi_2Te_3 crystal surface are shown in Fig. 6(e). Based on the results of the paper [4] we can expect that the band gap of Bi_2Te_3 in the Γ point is ~ 250 meV with the Dirac point position about 300 meV below the bottom of the conduction band. Given the minimal measured bulk hole and electron concentration to be on the order of 10^{17} cm^{-3} in the vicinity of the p-n junction, the Fermi level position should fall close to the valence band maximum and the conduction band minimum in the p and n parts of the crystal bulk, respectively. This means that there is a downward band bending of ~ 150 meV on the surface of

the p-Bi$_2$Te$_3$ region, comparable to the bulk band gap. In the case of the n-type surface, no emission from the conduction band states in the Γ point ($k_\parallel = 0$) is observed in the spectra, from which one can conclude the existence of a depletion region on the surface corresponding to a small upward band bending. The real barrier height at the p-n junction boundary can be estimated to be $\sim$10–20 meV, an order of magnitude less than expected. In both p and n parts of the crystal TSSs are filled with electrons, thus forming an almost barrierless TSS electron channel on the whole sample surface instead of the topological p-n junction.

A similar picture, despite the presence of a p-n transition in the bulk, is observed on the surface of the Bi$_{1.34}$Sb$_{0.66}$Te$_3$ [Figs. 6(c) and 6(d)]. However, the occupied states of the conduction zone (CB) are also observed. In the case of the p-Bi$_{1.34}$Sb$_{0.66}$Te$_3$ surface, these electronic states belong to the two-dimensional electron gas (2DEG) arising in the space charge region at the surface. Thus, the additional interface of the 2DEG to the bulk conduction band states is formed. The surface band bending for the Bi$_{1.34}$Sb$_{0.66}$Te$_3$ crystal is stronger compared to Bi$_2$Te$_3$, probably due to higher concentration of surface defects or different energy position of defects or the adsorbed atoms.

The presence of band bending at the surface can be explained either by adsorption of residual gases from the vacuum chamber [47,48] or Fermi level pinning on the "ordinary" surface states, caused by surface defects formed in the cleaving process or induced during measurements due to photon beam damage. A similar picture was reproduced after repeated cleaves of the sample surface, on different samples and on other experimental ARPES facilities. Despite the topological surface state being preserved at the surface, there is no topological p-n junction on the surface. It is known that the surface of perfect Bi$_2$Se$_3$ and Bi$_2$Te$_3$ single crystals remains inert to exposure to air for a long period of time [49,50], but adsorption of even a small volume of N$_2$ and O$_2$ leads to the appearance of a strong downward band bending even on the surface of n-type conductivity crystals. And accordingly, to study the properties of the topological surface state p-n junction it is required to additionally control the Fermi level position on the surface.

IV. CONCLUSIONS

Composition-graded Bi$_2$Te$_3$ and Bi$_{1.34}$Sb$_{0.66}$Te$_3$ single crystals with built-in lateral p-n transition were grown using the modified Bridgman method. The defect compensation naturally achieved at the p-n interface results in a strong reduction of the bulk carrier concentrations in both crystals. However, mixed hole and electron conductivity was observed in the areas close to the p-n junction, indicating strong chemical potential fluctuations in the crystals due to, probably, microscale composition inhomogeneity. Despite this fact, the crystals show unusually high carrier mobilities. In the Bi$_2$Te$_3$ crystal, a high-mobility n-type conductivity region is formed with an electron Hall mobility of 70 000 cm^2 V^{-1} s^{-1} and Hall concentration of 2×10^{18} cm^{-3} at 4.2 K, and a Seebeck coefficient of -350 µV/K at room temperature. As expected, high-mobility n-Bi$_2$Te$_3$ samples taken from this part of the crystal show prominent quantum resistivity oscillations at low temperatures. In the Bi$_{1.34}$Sb$_{0.66}$Te$_3$ crystal the region of intrinsic conductivity with the lowest observed hole Hall concentration of 6×10^{18} cm^{-3} and hole Hall mobility of 10 000 cm^2 V^{-1} s^{-1} is formed in the vicinity of the p-n junction. Thus, the composition grading can be used as a reliable method of obtaining high-quality single crystals with relatively large areas of low bulk carrier concentration and enhanced charge carrier mobility, which can be used in further nanoscale TI device fabrication. It can be noted that the composition grading used in this study should appear in any crystals of the studied materials grown using the same Bridgman growth process. It was shown using angle-resolved photoemission spectroscopy that downward band bending occurs on the surface of the p-type conductivity region of Bi$_2$Te$_3$ and Bi$_{1.34}$Sb$_{0.66}$Te$_3$ even in ultrahigh vacuum, providing an almost barrierless TSS electron channel on the whole sample surface instead of the topological p-n junction. This effect requires the Fermi level position on the surface to be additionally controlled in order to detect topological p-n junction related effects in future research. In addition, surface band bending in p-Bi$_{1.34}$Sb$_{0.66}$Te$_3$ causes formation of 2D electron gas, interfaced to the bulk conduction band states at the p-n junction border. It may be assumed that once the ideal p-n junction is formed in the bulk of the crystal, the current flow in the system in the p-n junction reverse direction should be maintained due to surface conductivity only.

ACKNOWLEDGMENT

[1] P. A. Walker, The thermal conductivity and thermoelectric power of bismuth telluride at low temperatures, Proc. Phys. Soc. London **76**, 113 (1960).

[2] D. M. Rowe, *Thermoelectrics Handbook: Macro to Nano* (CRC Press, Boca Raton, 2006).

[3] H. Zhang, C.-X. Liu, X.-L. Qi, X. Dai, Z. Fang, and S.-C. Zhang, Topological insulators in Bi$_2$Se$_3$, Bi$_2$Te$_3$ and Sb$_2$Te$_3$ with a single Dirac cone on the surface, Nat. Phys. **5**, 438 (2009).

[4] Y. L. Chen, J. G. Analytis, J.-H. Chu, Z. K. Liu, S.-K. Mo, X. L. Qi, H. J. Zhang, D. H. Lu, X. Dai, Z. Fang, S. C. Zhang, I. R. Fisher, Z. Hussain, and Z.-X. Shen, Experimental realization of a three-dimensional topological insulator, Bi$_2$Te$_3$, Science **325**, 178 (2009).

[5] Y. Xia, D. Qian, D. Hsieh, L. Wray, A. Pal, H. Lin, A. Bansil, D. Grauer, Y. S. Hor, R. J. Cava, and M. Z. Hasan, Observation of a large-gap topological-insulator class with a single Dirac cone on the surface, Nat. Phys. **5**, 398 (2009).

[6] X. L. Qi and S. C. Zhang, Topological insulators and superconductors, Rev. Mod. Phys. **83**, 1057 (2011).

[7] Y. Ando, Topological insulator materials, J. Phys. Soc. Jpn. **82**, 102001 (2013).

[8] F. Ortmann, S. Roche, and S. O. Valenzuela, *Topological Insulators: Fundamentals and Perspectives* (Wiley-VCH, Weinheim, Germany, 2015).

[9] D. O. Scanlon, P. D. King, R. P. Singh, A. D. L. Torre, S. M. K. Walker, G. Balakrishnan, F. Baumberger, and C. R. Catlow, Controlling bulk conductivity in topological insulators: Key role of anti-site defects, Adv. Mater. **24**, 2154 (2012).

[10] Y. Jiang, Y. Wang, M. Chen, Z. Li, C. Song, K. He, L. Wang, X. Chen, X. Ma, and Q.-K. Xue, Landau quantization and the thickness limit of topological insulator thin films of Sb_2Te_3, Phys. Rev. Lett. **108**, 016401 (2012).

[11] T. Chen, Q. Chen, K. Schouteden, W. Huang, X. Wang, Z. Li, F. Miao, X. Wang, Z. Li, B. Zhao, S. Li, F. Song, J. Wang, B. Wang, C. V. Haesendonck, and G. Wang, Topological transport and atomic tunnelling–clustering dynamics for aged Cu-doped Bi_2Te_3 crystals, Nat. Commun. **5**, 5022 (2014).

[12] T. Misawa, S. Nakamura, Y. Okazaki, Y. Fukuyama, N. Nasaka, H. Ezure, C. Urano, N. H. Kaneko, and T. Sasagawa, Dual-gate control of the surface carriers of the highly-bulk-resistive topological insulator $Sn_{0.02}Bi_{1.08}Sb_{0.9}Te_2S$, J. Phys.: Condens. Matter **32**, 405704 (2020).

[13] S. K. Kushwaha, Q. D. Gibson, J. Xiong, I. Pletikosic, A. P. Weber, A. V. Fedorov, N. P. Ong, T. Valla, and R. J. Cava, Comparison of Sn-doped and nonstoichiometric vertical-Bridgman-grown crystals of the topological insulator Bi_2Te_2Se, J. Appl. Phys. **115**, 143708 (2014).

[14] J. Zhang, C.-Z. Chang, Z. Zhang, J. Wen, X. Feng, K. Li, M. Liu, K. He, L. Wang, X. Chen, Q.-K. Xue, X. Ma, and Y. Wang, Band structure engineering in $(Bi_{1-x}Sb_x)_2Te_3$ ternary topological insulators, Nat. Commun. **2**, 574 (2011).

[15] D. Kong, Y. Chen, J. J. Cha, Q. Zhang, J. G. Analytis, K. Lai, Z. Liu, S. S. Hong, K. J. Koski, S. K. Mo, Z. Hussain, I. R. Fisher, Z. X. Shen, and Y. Cui, Ambipolar field effect in the ternary topological insulator $(Bi_xSb_{1-x})_2Te_3$ by composition tuning, Nat. Nanotechnol. **6**, 705 (2011).

[16] S. Jia, H. Ji, E. Climent-Pascual, M. K. Fuccillo, M. E. Charles, J. Xiong, N. P. Ong, and R. J. Cava, Low-carrier-concentration crystals of the topological insulator Bi_2Te_2Se, Phys. Rev. B **84**, 235206 (2011).

[17] J. Wang, X. Chen, B.-F. Zhu, and S.-C. Zhang, Topological *p-n* junction, Phys. Rev. B **85**, 235131 (2012).

[18] A. Banerjee, A. Sundaresh, S. Biswas, R. Ganesan, D. Sen, and P. S. A. Kumar, Topological insulator n-p-n junctions in a magnetic field, Nanoscale **11**, 5317 (2019).

[19] K. M. Masum Habib, R. N. Sajjad, and A. W. Ghosh, Chiral tunneling of topological states: Towards the efficient generation of spin current using spin-momentum locking, Phys. Rev. Lett. **114**, 176801 (2015).

[20] R. Ilan, F. de Juan, and J. E. Moore, Spin-based Mach-Zehnder interferometry in topological insulator $p-n$ junctions, Phys. Rev. Lett. **115**, 096802 (2015).

[21] Y. Xie, H. Vakili, S. Ganguly, and A. W. Ghosh, Anatomy of nanomagnetic switching at a 3D topological insulator PN junction, Sci. Rep. **13**, 9477 (2023).

[22] S. Datta and B. Das, Electronic analog of the electro-optic modulator, Appl. Phys. Lett. **56**, 665 (1990).

[23] N. Dai, Y.-F. Zhou, P. Lv, and Q.-F. Sun, Quantum transport through three-dimensional topological insulator *p-n* junction under magnetic field, Phys. Rev. B **98**, 085422 (2018).

[24] C. B. Satterthwaite and R. W. Ure, Electrical and thermal properties of Bi_2Te_3, Phys. Rev. **108**, 1164 (1957).

[25] H. Köhler, Non-parabolic $E(k)$ relation of the lowest conduction band in Bi_2Te_3, Phys. Status Solidi B **73**, 95 (1976).

[26] H. Köhler, Non-parabolicity of the highest valence band of Bi_2Te_3 from Shubnikov–de Haas effect, Phys. Status Solidi B **74**, 591 (1976).

[27] R. W. Ure Jr., High mobility n-type bismuth telluride, https://apps.dtic.mil/sti/pdfs/AD0410287.pdf (1962).

[28] K. A. Kokh, S. V. Makarenko, V. A. Golyashov, O. A. Shegai, and O. E. Tereshchenko, Melt growth of bulk Bi_2Te_3 crystals with a natural p-n junction, CrystEngComm **16**, 581 (2014).

[29] T. Bathon, S. Achilli, P. Sessi, V. A. Golyashov, K. A. Kokh, O. E. Tereshchenko, and M. Bode, Experimental realization of a topological p-n junction by intrinsic defect grading, Adv. Mater. **28**, 2183 (2016).

[30] G. Nakamoto and Y. Nakabayashi, Development of a two dimensional scanning Seebeck coefficient measurement system by a micro-probe method, Intermetallics **32**, 233 (2013).

[31] J. L. Mi, M. Bremholm, M. Bianchi, K. Borup, S. Johnsen, M. Søndergaard, D. Guan, R. C. Hatch, P. Hofmann, and B. B. Iversen, Phase separation and bulk p-n transition in single crystals of Bi_2Te_2Se topological insulator, Adv. Mater. **25**, 889 (2013).

[32] P. Lošťák, J. Horák, R. Novotný, and J. Klikorka, Monocrystalline structure of $Bi_2Te_3 - Bi_2Se_3$ with a p-n junction, J. Mater. Sci. Lett. **6**, 1469 (1987).

[33] S. H. Kim, K. H. Jin, B. W. Kho, B. G. Park, F. Liu, J. S. Kim, and H. W. Yeom, Atomically abrupt topological p-n junction, ACS Nano **11**, 9671 (2017).

[34] M. Eschbach, E. Młyńczak, J. Kellner, J. Kampmeier, M. Lanius, E. Neumann, C. Weyrich, M. Gehlmann, P. Gospodarič, S. Döring, G. Mussler, N. Demarina, M. Luysberg, G. Bihlmayer, T. Schäpers, L. Plucinski, S. Blügel, M. Morgenstern, C. M. Schneider, and D. Grützmacher, Realization of a vertical topological p-n junction in epitaxial Sb_2Te_3/Bi_2Te_3 heterostructures, Nat. Commun. **6**, 8816 (2015).

[35] D. Backes, D. Huang, R. Mansell, M. Lanius, J. Kampmeier, D. Ritchie, G. Mussler, G. Gumbs, D. Grützmacher, and V. Narayan, Disentangling surface and bulk transport in topological-insulator $p - n$ junctions, Phys. Rev. B **96**, 125125 (2017).

[36] N. H. Tu, Y. Tanabe, Y. Satake, K. K. Huynh, and K. Tanigaki, In-plane topological p-n junction in the three-dimensional topological insulator $Bi_{2-x}Sb_xTe_{3-y}Se_y$, Nat. Commun. **7**, 13763 (2016).

[37] K. A. Kokh, B. G. Nenashev, A. E. Kokh, and G. Y. Shvedenkov, Application of a rotating heat field in Bridgman-Stockbarger crystal growth, J. Cryst. Growth **275**, e2129 (2005).

[38] D. M. Rowe, *CRC Handbook of Thermoelectrics* (CRC Press, 1995).

[39] M. Yamamoto and N. Hamada, First-principles estimation of Seebeck coefficient of bismuth telluride and selenide, Jpn. J. Appl. Phys. **51**, 125601 (2012).

[40] M. Lang, L. He, X. Kou, P. Upadhyaya, Y. Fan, H. Chu, Y. Jiang, J. H. Bardarson, W. Jiang, E. S. Choi, Y. Wang, N. C. Yeh, J. Moore, and K. L. Wang, Competing weak localization and weak antilocalization in ultrathin topological insulators, Nano Lett. **13**, 48 (2013).

[41] M. M. Parish and P. B. Littlewood, Non-saturating magnetoresistance in heavily disordered semiconductors, Nature (London) **426**, 162 (2003).

[42] A. Narayanan, M. D. Watson, S. F. Blake, N. Bruyant, L. Drigo, Y. L. Chen, D. Prabhakaran, B. Yan, C. Felser, T. Kong, P. C. Canfield, and A. I. Coldea, Linear magnetoresistance caused by mobility fluctuations in n-doped Cd$_3$As$_2$, Phys. Rev. Lett. **114**, 117201 (2015).

[43] Z. D. Kvon, E. B. Olshanetsky, D. A. Kozlov, N. N. Mikhailov, and S. A. Dvoretsky, *Two-Dimensional Semimetal in HgTe-Based Quantum Wells* (Elsevier, 2017), pp. 29–48.

[44] M. V. Fischetti and S. E. Laux, Band structure, deformation potentials, and carrier mobility in strained Si, Ge, and SiGe alloys, J. Appl. Phys. **80**, 2234 (1996).

[45] F. Qu, C. Zhang, R.-R. Du, and L. Lu, Coexistence of bulk and surface Shubnikov–de Haas oscillations in Bi$_2$Se$_3$, J. Low Temp. Phys. **170**, 397 (2013).

[46] T. Chen, J. Han, Z. Li, F. Song, B. Zhao, X. Wang, B. Wang, J. Wan, M. Han, R. Zhang, and G. Wang, Shubnikov–de Haas quantum oscillation of the surface states in the metallic bismuth telluride sheets, Eur. Phys. J. D **67**, 75 (2013).

[47] H. M. Benia, C. Lin, K. Kern, and C. R. Ast, Reactive chemical doping of the Bi$_2$Se$_3$ topological insulator, Phys. Rev. Lett. **107**, 177602 (2011).

[48] P. D. C. King, R. C. Hatch, M. Bianchi, R. Ovsyannikov, C. Lupulescu, G. Landolt, B. Slomski, J. H. Dil, D. Guan, J. L. Mi, E. D. L. Rienks, J. Fink, A. Lindblad, S. Svensson, S. Bao, G. Balakrishnan, B. B. Iversen, J. Osterwalder, W. Eberhardt, F. Baumberger, and P. Hofmann, Large tunable Rashba spin splitting of a two-dimensional electron gas in Bi$_2$Se$_3$, Phys. Rev. Lett. **107**, 096802 (2011).

[49] V. V. Atuchin, V. A. Golyashov, K. A. Kokh, I. V. Korolkov, A. S. Kozhukhov, V. N. Kruchinin, I. D. Loshkarev, L. D. Pokrovsky, I. P. Prosvirin, K. N. Romanyuk, and O. E. Tereshchenko, Crystal growth of Bi$_2$Te$_3$ and noble cleaved (0001) surface properties, J. Solid State Chem. **236**, 203 (2016).

[50] V. A. Golyashov, K. A. Kokh, S. V. Makarenko, K. N. Romanyuk, I. P. Prosvirin, A. V. Kalinkin, O. E. Tereshchenko, A. S. Kozhukhov, D. V. Sheglov, S. V. Eremeev, S. D. Borisova, and E. V. Chulkov, Inertness and degradation of (0001) surface of Bi$_2$Se$_3$ topological insulator, J. Appl. Phys. **112**, 113702 (2012).